Asian Pub. Corp.

www.asianpubs.org

ARTICLE

Comparative Investigation of Some Selected Properties of Mn_3O_4/PbS and CuO/PbS Nanocomposites

C. Augustine[1,2,✉] and M.N. Nnabuchia[1]

Asian Journal of Materials Chemistry

Volume: 3 Year: 2018
Issue: 4 Month: October–December
pp: 72–78
DOI: https://doi.org/10.14233/ajmc.2018.AJMC-P67

Received: 12 September 2018
Accepted: 12 November 2018
Published: 8 December 2018

ABSTRACT

In this paper, a comparative study of Mn_3O_4/PbS and CuO/PbS nanocomposites deposited by chemical bath deposition method has been made using X-ray diffraction, scanning electron microscope, Rutherford back scattering, UV-visible spectroscopy and four point probe techniques. Structure of both nanocomposites were observed by XRD technique. The crystallite size for Mn_3O_4/PbS and CuO/PbS nanocrystalline films were found to be 34.86 nm and 19.14 nm, respectively. The surface morphology of both composites were observed by SEM technique. Mn_3O_4/PbS films showed non-uniform irregular spherical particles spread across the substrate surface, whereas CuO/PbS thin films showed uniform grains with dense structure which are well covered to the substrate with rod like structure. Both films have high absorbance exhibiting a maximum in the UV region. The direct band gaps of 3.90 and 3.95 eV were observed for Mn_3O_4/PbS and CuO/PbS films, respectively. The wide band gap values are in the range suitable for use as window materials in solar cell fabrication and high frequency applications.

KEYWORDS

Mn_3O_4/PbS, CuO/PbS, Grain size, Band gap, Nanocomposites.

INTRODUCTION

In recent years, semiconductor nanocrystalline films have been widely investigated due to the novel size dependent properties [1]. The main advantage of using nanomaterial is that it consists of very small particles. As they are small, nanostructures can be packed closely together. As a result, on a given unit area one can locate more functional nanodevices, which is very important for nanoelectronics [2]. Their high packing density has the potential to bring high area and volume capacity to information storage and higher speed of information processing [3]. In view of technical applications, the optical properties of nanoparticles and nanocomposites are of major interest. Besides their economic, the scientific background of these properties is of fundamental importance in order to understand the behaviour of nanomaterials [4].

The survey of literature showed that the synthesis of core/shell heterostructures has gained recognition due to the synergetic properties or complementary behaviours offered by the composite nanostructures. There are many studies on the synth-

Author affiliations:

[1]Department of Physics/Geology/Geophysics, Alex Ekwueme Federal University Ndufu-Alike Ikwo, Ikwo, Ebonyi State, Nigeria
[2]Department of Industrial Physics, Ebonyi State University, Abakaliki, Ebonyi State, Nigeria

✉To whom correspondence to be addressed:

E-mail: emmyaustine2003@yahoo.com

Available online at: http://ajmc.asianpubs.org

esis of various core/shell heterostructures such as semiconductor/semiconductor [5], semiconductor/metal [6], metal/metal oxide [7], metal/metal [8], metal oxide/metal oxide [9], metal oxide/conductive polymer [10] have been explored, and enhanced properties have been demonstrated. However, research work on oxide/sulphide core-shell thin films is limited [11-15]. We contribute by successfully fabricating Mn_3O_4/PbSand CuO/PbS nanocompositeson plane glass substrates using chemical bath deposition technique, with emphasis on the structural, morphological, optical and solid state properties of the nanocomposites.

EXPERIMENTAL

Synthesis of Mn_3O_4/PbS nanocomposite: The chemical bath for the deposition of Mn_3O_4 was made up of a mixture of 12 mL of 1 M $MnCl_4$, 12 mL of 1 M NH_4Cl, 12 mL of 100 % NH_3 and 24 mL of distilled water. Five clean glass slides were then inserted vertically into the solution. The deposition was allowed to proceed at 80 ºC for 5 h after which the coated substrates were removed, washed with distilled water and allowed to dry. The deposited Mn_3O_4 was inserted in a mixture containing 5 mL of 0.2 M $Pb(NO_3)_2$, 5 mL of 1 M thiourea, 5 mL of 1 M NaOH and 35 mL of distilled water put in that order in 100 mL cleaned and dried beaker for 50 min to form Mn_3O_4/PbS core-shell thin film. One sample of the deposited films was selected for characterization.

Synthesis of CuO/PbS nanocomposite: The chemical bath for the deposition of CuO was made up of a mixture of 4 mL of 1 M $CuSO_4$, 4 mL of 1 M KCl, 2 mL of 100 % NH_3 and 13 mL of distilled water. The deposition took place at 80 ºC bath temperature for 3 h. To deposit CuO/PbS films, the deposited CuO films were inserted into a mixture containing 5 mL of 0.2 M $Pb(NO_3)_2$, 5 mL of 1 M thiourea, 5 mL of 1 M NaOH and 35 mL of distilled water put in that order in 50 mL beaker for 50 min.

Characterization: Optical absorption data were obtained with a thermo-scientific GENESYS 10S model UV-VIS spectrophotometer at normal incidence of light in the wavelength range of 300-1000 nm. Proton induced X-ray emission (PIXE) scans on the samples from a Tandem Accelerator Model 55DH 1.7MV Pellaton by National Electrostatic Corporation (NEC), USA, which effectively performed Rutherford back scattering (RBS) elemental characterizations on both deposits and substrates. The RBS also deciphered the thicknesses of film deposits. The crystal structure and phase analysis of the deposited film was carried out at room temperature with an X-ray diffractrometer Rigaku Ultima IV model, using gracing incident at 30 mA, 40 KV with CuK_α radiation of wavelength $\lambda = 0.15406$ nm. Scanning electron micrscope (Tescan model) was used to observe the morphology of deposited core-shell thin films.

RESULTS AND DISCUSSION

X-ray diffraction analysis: The grown nanocomposites were characterized by powder X-ray diffractometer. Fig. 1(a-b) shows the X-ray diffraction spectra of Mn_3O_4/PbS and CuO/PbS thin films, respectively. The strong peak intensity indicates the high degree of crystallinity of the films. The presence of more than one peak indicates that both films are polycrystalline.

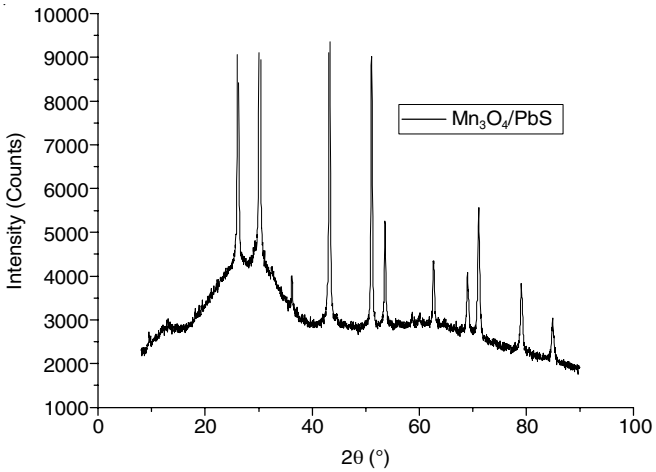

Fig. 1(a). XRD patterns of Mn_3O_4/PbS nanoconposites

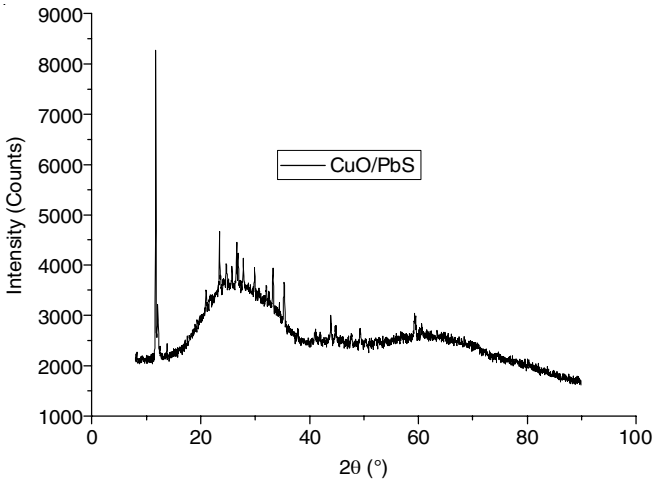

Fig. 1(b). XRD patterns of CuO/PbS nanoconposites

Different diffraction patterns can be observed for both nanocomposites. Comparative study of XRD patterns of both films showed that Mn_3O_4/PbS films exhibited more intense peaks compared to CuO/PbS films.The average grain sizes of 34.86 and 19.14 nm were observed for Mn_3O_4/PbS and CuO/PbS films, respectively. The microstrain of both films which is related to the lattice misfit and depends on the deposition conditions was calculated as 0.1020 and 0.1039 for Mn_3O_4/PbS and CuO/PbS films, respectively.

The average crystallites sizes D in both nanocomposites was deduced from the Scherrer's equation [16,17]:

$$D = \frac{K\lambda}{\beta\cos\theta} \quad (1)$$

The microstrain (ε) produced in the nanocomposites was calculated using the equation below [18]:

$$\mu = \frac{\beta\cos\theta}{4} \quad (2)$$

where β is the peak width at mid height, θ is the diffraction angle, K is a constant and equal to 0.9, the constant $\lambda = 0.15406$ nm, D is the grain size and ε represent strains in the film.

Surface morphological analysis: The SEM images of Mn_3O_4/PbS and CuO/PbS nanocomposites are shown in Fig. 2a and 2b, respectively. Fig. 2a depicts a non-uniform irregular spherical grains scattered across the substrate surface with few

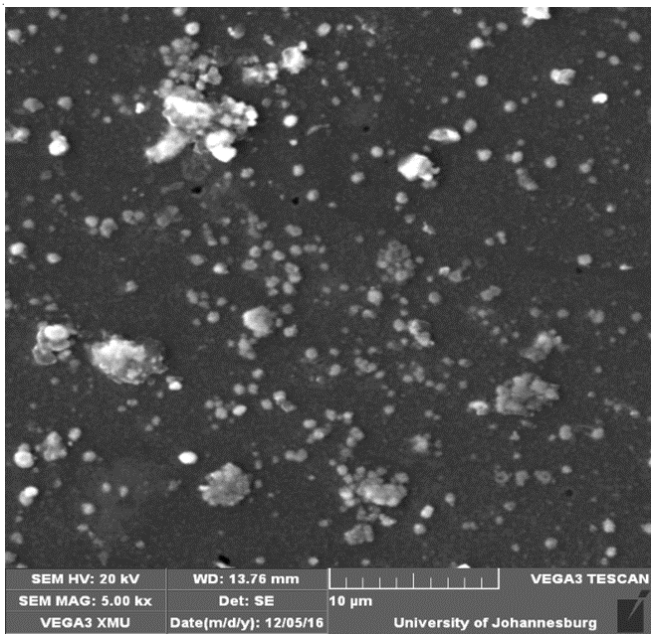

Fig. 2(a). SEM images of Mn_3O_4/PbS nanocomposites

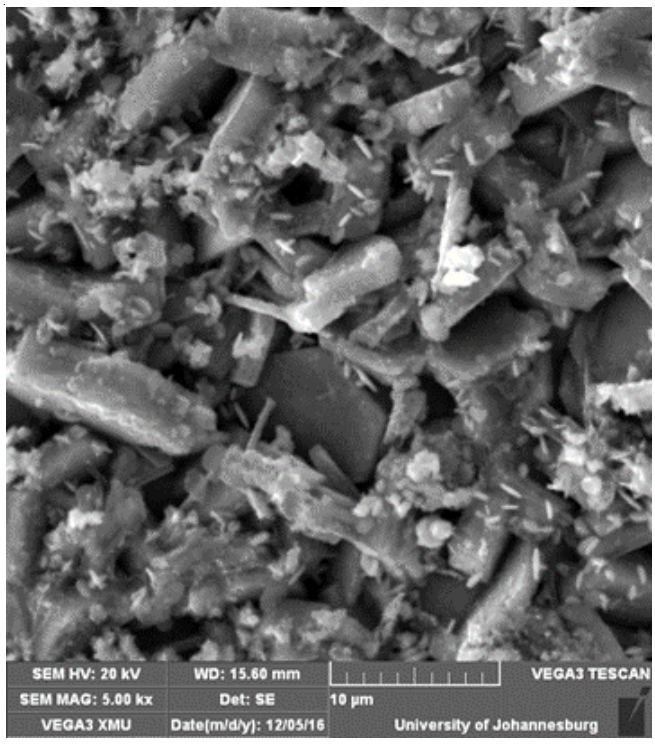

Fig. 2(b). SEM images of CuO/PbS nanocomposites

pin-holes. Fig. 2b shows particles engaged in a flower-like rod structure indicating the nanocrystalline nature of CuO/PbS thin film. The observed long network of structure ordering makes CuO/PbS film good material for design of light-trapping configuration for solar cells [19].

Elemental composition analysis: The elemental composition of the films was carried out using Rutherford backscattering technique. The percentage composition of Mn_3O_4/PbS and CuO/PbS thin films are presented in Tables 1 and 2, respectively. In RBS analysis, film thickness is determined by the width of peak, while concentration is determined by the intensity or height of the peak. The thickness of the films as deciphered by RBS are 1026 and 650 nm for Mn_3O_4/PbS and CuO/PbS films, respectively. The eqn. 3 [20] was also used to calculate the thickness of film in order to compare with that deciphered by RBS technique. The calculated thicknesses of Mn_3O_4/PbS and CuO/PbS films are in conformity with the RBS result. Fig. 3a-b shows the RBS micrographs of Mn_3O_4/PbS and CuO/PbS thin films, respectively.

$$t = \frac{\left[\tan^{-1}\left(\frac{(n_o+n_g)^2R-(n_o-n_g)^2}{\left(\frac{n_on_g}{n}-n\right)^2-\left(\frac{n_on_g}{n}+n\right)^2R}\right)^{\frac{1}{2}}\lambda\right]}{2\pi n} \quad (3)$$

where t is thickness, n_o is the refractive index of medium of the incident light, which in this study is air, n_g is the refractive index of the substrate (glass in this case); and n is the refractive index of thin film, R is reflectance and λ is wavelength.

Optical properties: The optical absorption and transmission spectra of Mn_3O_4/PbS and CuO/PbS composites deposited on transparent glass recorded in wavelength range 300-1000 nm are shown in Figs. 4 and 5 respectively. Mn_3O_4/PbS film exhibited peak absorbance of about 1.40 a.u. whereas CuO/PbS exhibited peak absorbance of about 1.70 a.u. Both peaks occurred in the UV region. A significant difference in the absorption peak is observed. The absorption edge for Mn_3O_4/PbS film occurred at about 0.40 a.u. corresponding to about 325 nm whereas CuO/PbS film exhibited absorption edge at about 0.65 a.u. correspond to about 340 nm. The absorbance of both films are higher in the UV region with a sharp decrease in the visible and near infrared regions. The absorbance of CuO/PbS nanocomposite is generally higher in the UV region compared

TABLE-1
PERCENTAGE COMPOSITION OF Mn_3O_4/PbS NANOCOMPOSITE

Sample	Pb	Fe	Mn	Ca	K	S	Si	Al	Na	O
Glass slide	–	0.30	–	6.00	3.50	–	34.00	5.20	25.00	26.00
Mn_3O_4/PbS	70.63	–	17.78	–	–	29.33	–	–	–	82.22

TABLE-2
PERCENTAGE COMPOSITION OF CuO/PbS NANOCOMPOSITE

Sample	Pb	Cu	Fe	Ca	K	S	Si	Al	Na	O
Glass slide	–	–	0.30	6.00	3.50	–	34.00	5.20	25.00	26.00
Mn_3O_4/PbS	0.59	5.64	–	–	–	33.16	–	–	–	94.36

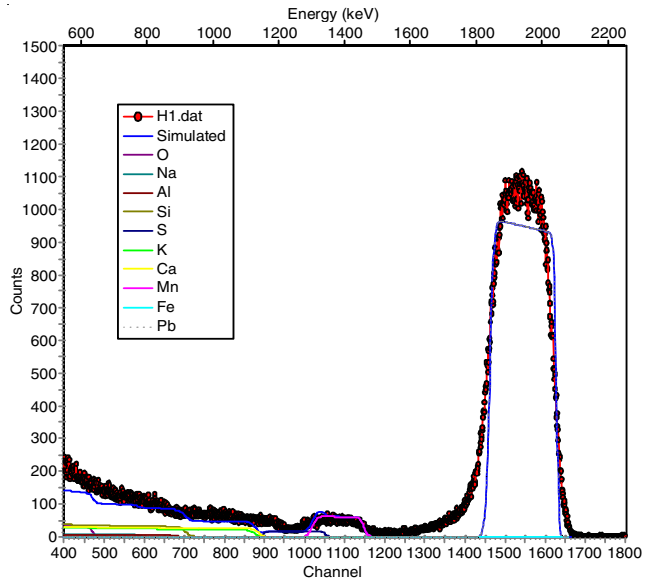

Fig. 3(a). Rutherford back scattering micrograph of Mn_3O_4/PbS thin film

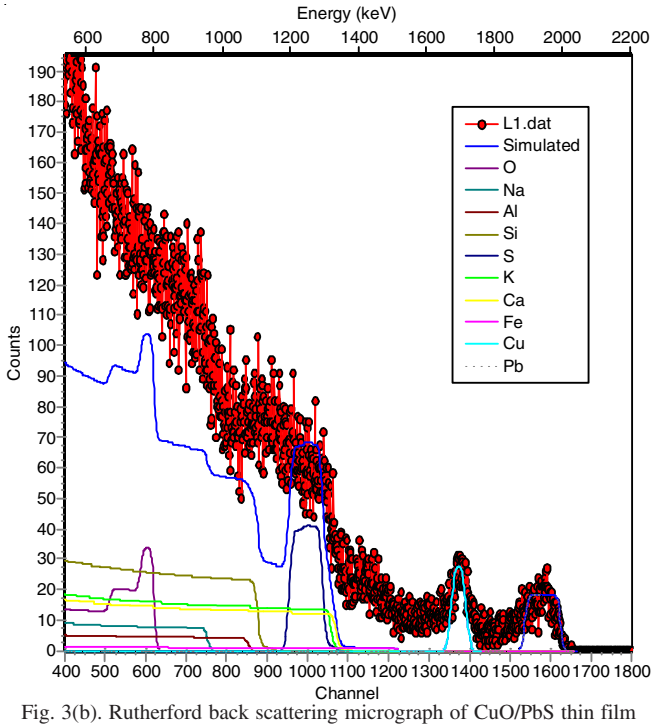

Fig. 3(b). Rutherford back scattering micrograph of CuO/PbS thin film

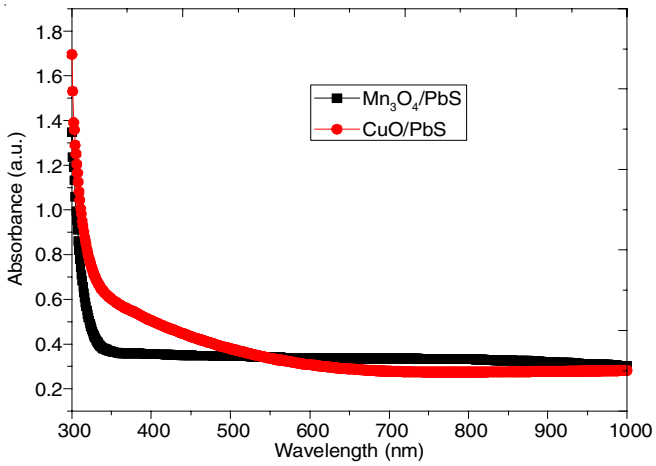

Fig. 4. Optical absorbance of Mn_3O_4/PbS and CuO/PbS composites

to Mn_3O_4/PbS nanocomposite. From Fig. 5, Mn_3O_4/PbS films transmit more than CuO/PbS films in the UV region. However, in the visible and infrared regions, CuO/PbS films transmit higher than Mn_3O_4/PbS films. Generally, Mn_3O_4/PbS nanocomposite transmit below 50 %, whereas CuO/PbS nanocomposite transmit above 50 %. Fig. 6 depicted the plots of reflectance against wavelength for Mn_3O_4/PbS and CuO/PbS nanostructures. It is observed that the reflectance of both films vary in similar manner. However, Mn_3O_4/PbS naocomposite shows higher reflectance in the entire electromagnetic region compared to CuO/PbS nanocomposite.

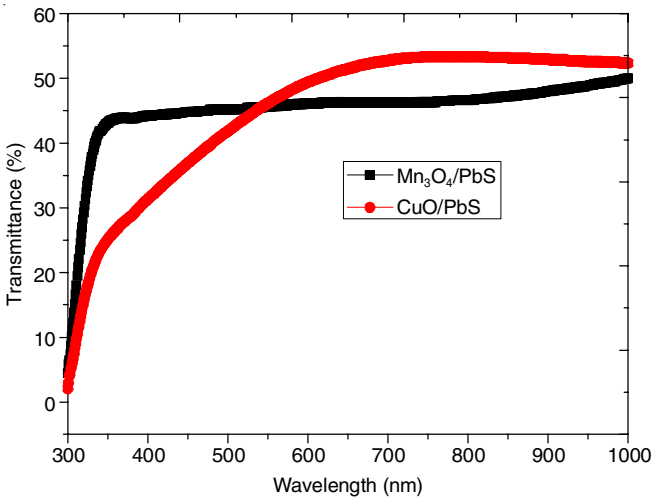

Fig. 5. Optical transmittance of Mn_3O_4/PbS and CuO/PbS composites

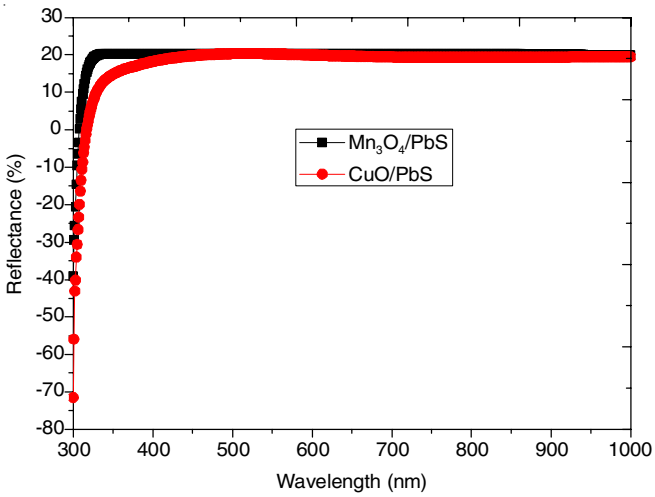

Fig. 6. Reflectance (R) against wavelength of Mn_3O_4/PbS and CuO/PbS composites

The transmittance (T), reflectance (R), absorption coefficient (α) and band gap (E_g) were calculated from the following relations [21]:

$$T = (1 - R^2)\exp(-A) \quad (4)$$

$$R = 1 - [T\exp(A)]^{1/2} \quad (5)$$

$$\alpha = \frac{1}{t}\ln\frac{(1-R^2)}{T} \quad (6)$$

$$(\alpha h\nu)^n = A(h\nu - E_g) \quad (7)$$

where A is band edge parameter and value of n determines the nature of optical transition (n = ½ indicates direct transition and n = 2 indicates indirect transition).

The plots of absorption coefficient as a function of photon energy for both nanocomposites are presented in Fig. 7. The absorption coefficients of Mn_3O_4/PbS and CuO/PbS composites vary in a similar manner, increasing from 0.75×10^6 m^{-1} at 1.23 eV to a maximum of 2.75×10^6 m^{-1} at 4.25 eV for Mn_3O_4/PbS nanocomposite, and 1.1×10^6 m^{-1} at 1.23 eV to a maximum of 6.25×10^6 m^{-1} at 4.25 eV for CuO/PbS nanocomposite. In general, Mn_3O_4/PbS nanocomposite exhibited lower absorption coefficient values compared to CuO/PbS nanocomposite. The absorption coefficients of both films increased with increasing photon energy (decreasing wavelength).

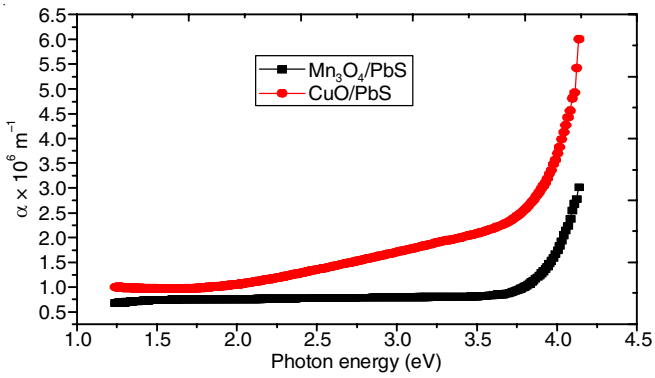

Fig. 7. Plots of absorption coefficient as a function of photon energy

Fig. 8 depicted the plots of product of absorption coefficient and photon energy square $(\alpha h\nu)^2$ against photon energy ($h\nu$). The extrapolation of straight line portion of $(\alpha h\nu)^2$ against $h\nu$ to energy axis for zero absorption coefficient gave optical band gap energy value as 3.90 and 3.95 eV for Mn_3O_4/PbS and CuO/PbS nanocomposites, respectively. The values for Mn_3O_4 as widely reported is 3.07-3.55 eV [22,23] while that of CuO is 1.90-2.91 eV [24,25]. It can be seen that the formation of Mn_3O_4/PbS and CuO/PbS nanocomposites shifted the fundamental absorption edge of core binary origin, thus providing tuning effect to the band gap for special applications. The primary function of a window layer in a heterojunctionas reported in literature is to form a junction with the absorber layer while admitting a maximum amount of light to the junction region and the absorber layer. The wide direct band gaps of the films placed them as suitable materials for window layers in solar cell fabrication.

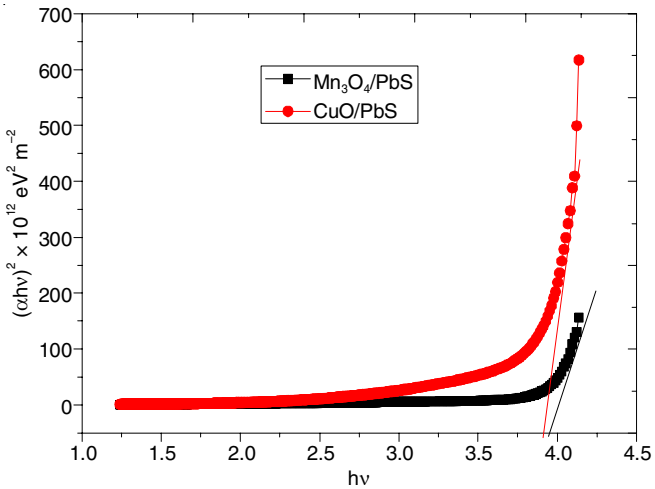

Fig. 8. Plots of $(\alpha h\nu)^2$ against photon energy ($h\nu$) for Mn_3O_4/PbS and CuO/PbS composites

The refractive index (n), extinction coefficient (k), optical conductivity (σ_o), real dielectric constant (ε_r), imaginary dielectric constant (ε_i), electrical conductivity (σ_e) and thermal conductivity (σ_t) were calculated using the relations available in literature [26,27].

$$n = \frac{1+R}{1-R} + \sqrt{\frac{4R}{(1+R^2)} - k^2} \quad (8)$$

$$k = \sqrt{\left(\frac{1}{2}\left\{\varepsilon_r^2 + \varepsilon_i^2\right\}^{1/2} - \frac{\varepsilon_r}{2}\right)} \quad (9)$$

$$\sigma_o\ (s^{-1}) = \frac{\alpha nc}{4\pi} \quad (10)$$

$$\varepsilon_r = n^2 - k^2 \quad (11)$$

$$\varepsilon_i = 2\ ink \quad (12)$$

$$\sigma_e\ (\Omega m)^{-1} = \frac{2\pi}{\lambda nc} \quad (13)$$

$$\sigma_t = \frac{\sigma_e \pi^2}{3\left(\frac{K_B}{e}\right)^2} T \quad (14)$$

Fig. 9 shows the plots of refractive index as a function of photon energy for Mn_3O_4/PbS and CuO/PbS nanocomposites while Fig. 10 depicted the extinction coefficient plots against photon energy. Fig. 9 showed that the refractive index increased with increasing photon energy (decreasing wavelength) with a sharp decrease at 3.75 and 3.00 eV for Mn_3O_4/PbS and CuO/PbS nanocomposites, respectively. The extinction coefficients of both films vary in the same manner in the UV and infrared regions. However, different behaviour is observed in the visible region. It decreased with photon energy in the visible region for Mn_3O_4/PbS film, whereas it increased with photon energy in the same region for CuO/PbS film. Generally, Mn_3O_4/PbS nanocomposite showed lower values of extinction coefficients compared to CuO/PbS nanocomposite.

The plots of optical conductivity as a function of photon energy (Fig. 11) shows that Mn_3O_4/PbS and CuO/PbS nanocomposites behaviour differently in the infrared region *i.e.* it increased with photon energy for Mn_3O_4/PbS nanocomposite, whereas it decreased with photon energy for CuO/PbS nanocomposite. However, in UV and visible regions, both films exhibited similar behaviour. We observed that the real dielectric constant (Fig. 12) and refractive index (Fig. 9) vary in a similar manner with photon energy. Such behaviour has been reported by other authors [20,28-30]. The imaginary dielectric plots as a function of photon energy is shown in Fig. 13. Mn_3O_4/PbS film has higher values of imaginary dielectric compared to CuO/PbS film. However, both films showed similar behaviour in the UV and IR regions. Fig. 14 depicted the plots of thermal conductivity as a function of photon energy of Mn_3O_4/PbS

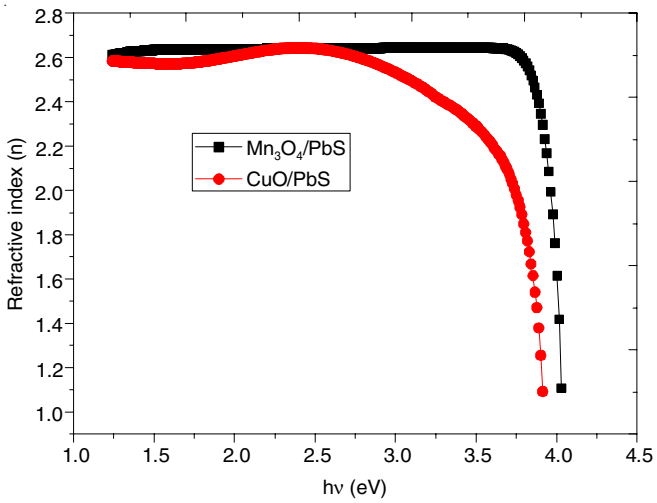

Fig. 9. Plots of refractive index (n) against photon energy (hν) for Mn_3O_4/PbS and CuO/PbS composites

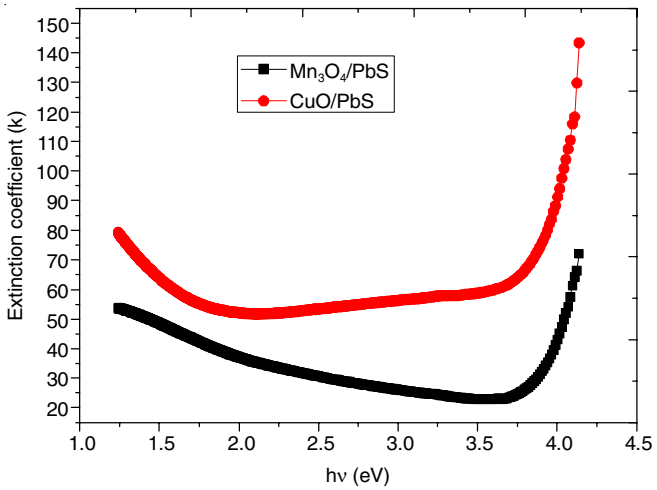

Fig. 10. Plots k against (hν) for Mn_3O_4/PbS and CuO/PbS composites

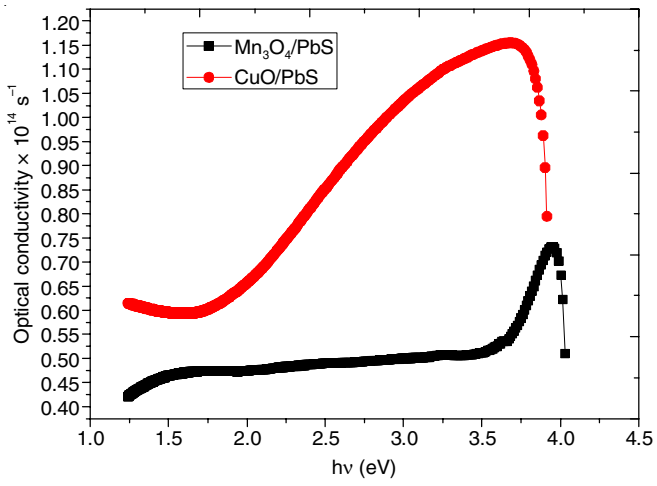

Fig. 11. Plots of optical conductivity against photon energy

and CuO/PbS composites. Both films exhibited similar behaviour across the entire spectrum reaching a maximum in the UV region. An increasing trend of thermal conductivity with increasing photon energy (decreasing wavelength) was observed for both films.

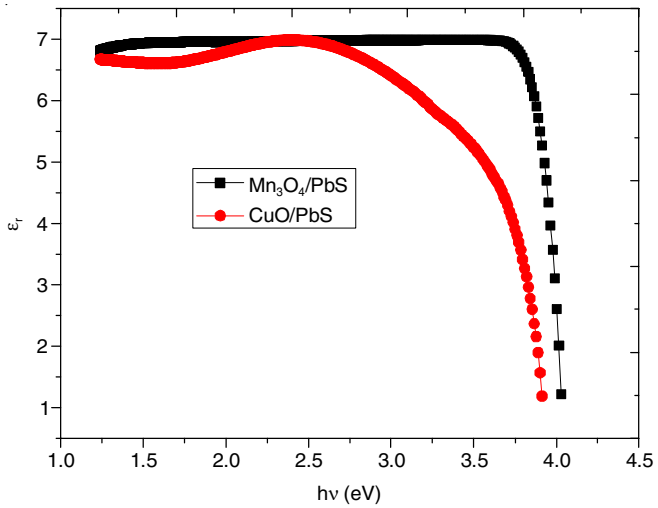

Fig. 12. Plots of real dielectric constant (ε_r) against photon energy (hν)

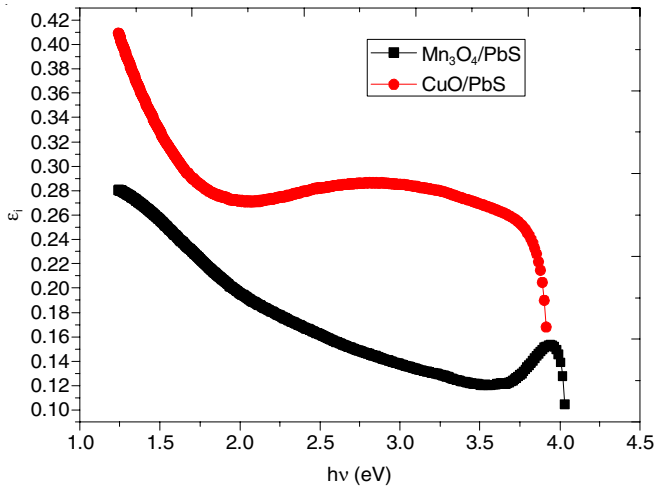

Fig. 13. Plots of real dielectric constant (ε_i) against photon energy (hν)

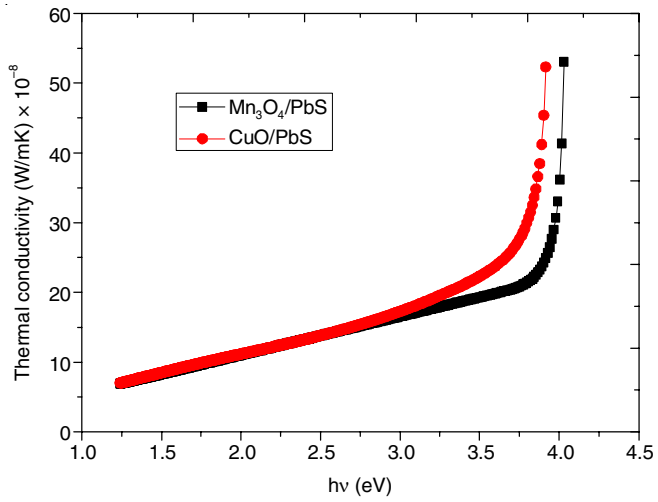

Fig. 14. Plots of thermal conductivity against photon energy (hν)

Conclusion

Mn_3O_4/PbS and CuO/PbS nanocomposites were successfully coated on the glass substrate using chemical bath deposition technique. The structural, morphological, optical and solid state properties of the prepared films were analyzed. Both nanocomposites varied considerably with the structural, morph-

ological, optical and solid state parameters. Both composites are semiconductors with different wide direct band gaps suitable for use as window materials in heterojunction solar cell, optoelectronic devices and high frequency applications.

REFERENCES

1. P. Nemec, I. Nemec, P. Nahálková, K. Knízek and P. Malý, Ammonia Free Chemical Bath Deposition of CdS Films: Tailoring The Nanocrystal Sizes, *J. Cryst. Growth*, **240**, 484 (2002); https://doi.org/10.1016/S0022-0248(02)00930-2.
2. G. Korotcenkov, Chemical Sensors: Nanostructured Materials, Momentum Press: New York (2010).
3. R. Chandran, Ph.D. Thesis, Synthesis and Characterization of Metal Chalcogenide Nanocrystalline Films, Department of Physics, Annamalai University, India (2011).
4. M. Quinten, Optical Properties of Nanoparticle Systems, Wiley-VCH, (2011).
5. M. Ben-Ishai and F. Patolsky, A Route to High-Quality Crystalline Coaxial Core/Multishell Ge@Si(GeSi)$_n$ and Si@(GeSi)$_n$ Nanowire Heterostructures, *Adv. Mater*., **22**, 902 (2010); https://doi.org/10.1002/adma.200902815.
6. Y. Wu, J. Xiang, C. Yang, W. Lu and C.M. Lieber, Single-Crystal Metallic Nanowires and Metal/Semiconductor Nanowire Heterostructures, *Nature*, **430**, 61 (2004); https://doi.org/10.1038/nature02674.
7. P.Y. Keng, M.M. Bull, I.B. Shim, K.G. Nebesny, N.R. Armstrong, Y. Sung, K. Char and J. Pyun, Colloidal Polymerization of Polymer-Coated Ferromagnetic Cobalt Nanoparticles into Pt-Co_3O_4 Nanowires, *Chem. Mater.*, **23**, 1120 (2011); https://doi.org/10.1021/cm102319d.
8. C. Koenigsmann, A.C. Santulli, K.P. Gong, M.B. Vukmirovic, W.P. Zhou, E. Sutter, S.S. Wong and R.R. Adzic, Enhanced Electrocatalytic Performance of Processed, Ultrathin, Supported Pd-Pt Core-Shell Nanowire Catalysts for the Oxygen Reduction Reaction, *J. Am. Chem. Soc.*, **133**, 9783 (2011); https://doi.org/10.1021/ja111130t.
9. Y.L. Chueh, I.J. Chou and Z.L. Wang, SiO_2/Ta_2O_5 Core-Shell Nanowires and Nanotubes, *Angew. Chem*., **45**, 7773 (2006); https://doi.org/10.1002/anie.200602228.
10. R. Liu and S.B. Lee, MnO_2/Poly(3,4-ethylenedioxythiophene) Coaxial Nanowires by One-Step Co-Electrodeposition for Electrochemical Energy Storage, *J. Am. Chem. Soc.*, **130**, 2942 (2008); https://doi.org/10.1021/ja7112382.
11. P. Kundu, P.A. Deshpande, G. Madras and W. Ravishankar, Nanoscale ZnO/CdS Heterostructure with Engineered Interfaces for High Photocatalytic Activity under Solar Radiation, *J. Mater. Chem.*, **21**, 4209 (2011); https://doi.org/10.1039/c0jm03116j.
12. T. Ghrib, M.A. Al-Messiere and A.L. Al-Otaibi, Synthesis and Characterization of ZnO/ZnS Core-Shell Nanowires, *J. Nanomater.*, Article ID 989632 (2014); https://doi.org/10.1155/2014/989632.
13. Z. Braiek, A. Brayek, M. Ghoul, S. Ben Taieb, M. Gannouni, I. Ben Assaker, A. Souissi and R. Chtourou, Electrochemical Synthesis of ZnO/In_2S_3 Core-Shell Nanowires for Enhanced Photoelectrochemical Properties, *J. Alloys Compd.*, **653**, 395 (2015); https://doi.org/10.1016/j.jallcom.2015.08.204.
14. C. Augustine, M.N. Nnabuchi, F.N.C. Anyaegbunam and A.N. Nwachukwu, Study of the Effects of Thermal Annealing on Some Selected Properties of Heterojunction PbS-NiO Core-Shell Thin Film, *Dig. J. Nanomater. Biostruct.*, **12**, 523 (2017).
15. C. Augustine and M.N. Nnabuchi, Band Gap Determination of Novel PbS-NiO-CdO Heterojunction Thin Film for Possible Solar Energy Applications, *J. Ovonic Res.*, **13**, 233 (2017).
16. H.P. Klug and L.E. Alexander, X-ray Diffraction Procedure for Polycrystalline and Armophous Materials, Wiley: New York (1974).
17. H. Jensen, J.H. Pedersen, J.E. Jorgensen, J.S. Pedersen, K.D. Joensen, S.B. Iversen and E.G. Sogaard, Determination of Size Distributions in Nanosized Powders by TEM, XRD and SAXS, *J. Exp. Nanosci.*, **1**, 355 (2006); https://doi.org/10.1080/17458080600752482.
18. K.O. Ovid'ko, Interfaces and Misfit Defects in Nanostructured and Polycrystalline Films, *Rev. Adv. Mater. Sci.*, **1**, 61 (2000).
19. T. Soga, Fundamentals of Solar Cell Nanostructured Materials for Solar Energy Conversion, Elsevier: UK, pp. 3-4 (2006).
20. M.N. Nnabuchi, Bandgap and Optical Properties of Chemical Bath Deposited Magnesium Sulphide (MgS) Thin Films, *Pacific J. Sci. Technol.*, **6**, 105 (2005).
21. C.D. Lokhande, B.R. Sankapal, S. Mane, H.M. Pathan, M. Muller, M. Giersig and V. Ganesan, XRD, SEM, AFM, HRTEM, EDAX and RBS Studies of Chemically Deposited Sb_2S_3 and Sb_2Se_3 Thin Films, *Appl. Surf. Sci.*, **193**, 1 (2002); https://doi.org/10.1016/S0169-4332(01)00819-4.
22. H.Y. Xu, S. Xu, H. Wang and H. Yan, Characterization of Hausmannite Mn_3O_4 Thin Films by Chemical Bath Deposition, *J. Electrochem. Soc.*, **152**, C803 (2005); https://doi.org/10.1149/1.2098267.
23. C. Ulutas, O. Erken, M. Gunes and C. Gumus, Effect of Annealing Temperature on the Physical Properties of Mn_3O_4 Thin Film Prepared By Chemical Bath Deposition, *Int. J. Electrochem. Sci.*, **11**, 2835 (2016); https://doi.org/10.20964/110402835.
24. S.S. Shariffudin, S.S. Khalid, N.M. Sahat, M.S.P. Sarah and H. Hashim, Preparation and Characterization of Nanostructured CuO Thin Films using Sol-Gel Dip Coating, *IOP Conf. Series Mater. Sci. Eng.*, **99**, 012007 (2015); https://doi.org/10.1088/1757-899X/99/1/012007.
25. K.S. Wanjala, W.K. Njoroge, N.E. Makori and J.M. Ngaruiya, Optical and Electrical Characterization of CuO Thin Films as Absorber Materials for Solar Cell Applications, *Am. J. Conden. Matter Phys.*, **6**, 1 (2016); https://doi.org/10.5923/j.ajcmp.20160601.01.
26. J.I. Pankove, Optical Processes in Semiconductors, Prentice-Hall: New York (1971).
27. C.C. Uhuegbu, Ph.D Thesis, Growth and Characterization of Ternary Chalcogenide Thin Films for Efficient Solar Cells and Possible Industrial Applications, Department of Physics, Covenant University, Ota, Ogun State, Nigeria (2007).
28. P.E. Agbo and M.N. Nnabuchi, Core-Shell TiO_2/ZnO Thin Film: Preparation, Characterization and Effect of Temperature on Some Selected Properties, *Chalcogenide Lett.*, **8**, 273 (2011).
29. P.E. Agbo, Refractive Index and Dielectric Properties of TiO_2/CuO Core-Shell Thin Films, *Chem. Mater. Res.*, **6**, 42 (2014).
30. C.E. Ekuma, M.N. Nnabuchi, E. Osarolube, E.O. Chukwuocha and M.C. Onyeaju, Optoelectronic Characterization of Chemical Bath Deposited $Cd_xCo_{1-x}S$ Thin Film, *J. Mod. Phys.*, **2**, 992 (2011); https://doi.org/10.4236/jmp.2011.29119.